CMS Physics Analysis Summary

Contact: cms-pag-conveners-higgs@cern.ch 2016/10/12

Search for charged Higgs bosons with the $H^{\pm} \to \tau^{\pm}\nu_{\tau}$ decay channel in the fully hadronic final state at $\sqrt{s} = 13$ TeV

The CMS Collaboration

Abstract

A search for charged Higgs bosons in decays of $H^{\pm} \to \tau^{\pm}\nu_{\tau}$ is presented both with mass larger than the top quark in the $pp \to H^{\pm}tb$ production process, and lighter than the top quark in the $pp \to H^{\pm}W^{\mp}b\bar{b}$ channel. The fully hadronic final state is considered. The search is performed using the 2016 data collected by CMS at $\sqrt{s} = 13$ TeV, and that correspond to a total integrated luminosity of 12.9 fb^{-1}. The observation agrees with the standard model prediction. Limits on the charged Higgs boson cross section times branching fraction are set for the mass range of 180 GeV $< m_{H^{\pm}} <$ 3 TeV, while limits on the branching fraction of top quark to charged Higgs boson are set in the mass range of 80 to 160 GeV, and results are interpreted in the context of two-Higgs-doublet models.

1 Introduction

During Run I, the ATLAS and CMS collaborations discovered a neutral Higgs boson with $m_{\mathrm{H}} = 125.09 \pm 0.21(\mathrm{stat.}) \pm 0.11(\mathrm{syst.})$ GeV [1, 2], compatible with a standard model (SM) Higgs boson [3–11]. The discovery of a further scalar boson, neutral or charged, would represent unambiguous evidence for an extended Higgs sector. Charged Higgs bosons appear in many extensions of the SM with at least two Higgs doublets, of which the simplest are the two-Higgs-doublet models (2HDM) [12, 13]. Five Higgs bosons are predicted in 2HDM: the light and heavy CP-even Higgs bosons h and H, the CP-odd Higgs boson A, plus two charged Higgs bosons $\mathrm{H}^{\pm}$. The 2HDM models can be classified depending on the Higgs boson coupling to fermions. In the so-called Type-I 2HDM only one of Higgs doublet couples to fermions while in a Type-II 2HDM one doublet couples to up-type fermions and the other to down-type fermions. This has as consequence that the coupling of the charged Higgs bosons to charged leptons and neutrinos is proportional to $\cot\beta$ in Type-I 2HDM and to $\tan\beta$ in Type-II 2HDM, where $\tan\beta$ is the ratio of the vacuum expectation values of the two Higgs boson doublets. The minimal supersymmetric standard model (MSSM) [14] is a special case of a Type-II 2HDM scenarios. Charged Higgs bosons are also predicted by models with a more complicated Higgs sector, such as Higgs triplet models [15, 16].

Experiments at the large electron-positron collider conducted searches for charged Higgs boson setting limits setting a model-independent lower bound on the mass of $\mathrm{H}^{\pm}$ of 80 GeV (72.5 GeV) for Type-II (Type-I) models [17]. Searches at the Tevatron [18, 19] and the LHC Run-I [20] extended the limits to large masses. Searches in Run-I resulted in model independent limits from $m_{\mathrm{H}^{\pm}} = 200$ GeV up to $m_{\mathrm{H}^{\pm}} = 600$ GeV, excluding a production cross section of 0.37–0.025 pb depending on the mass. For the light charged Higgs, the production limits from $m_{\mathrm{H}^{\pm}} = 80$ GeV to $m_{\mathrm{H}^{\pm}} = 160$ GeV, excluding a production cross section at $\sqrt{s} = 8$ TeV of 12.–1.5 fb.

This summary describes the search of a charged Higgs boson in decays to a tau lepton and a neutrino based on 12.9 fb^{-1} recorded in 2016 at $\sqrt{s} = 13$ TeV. The analysis considers the production mode $\mathrm{pp} \to \mathrm{tbH}^{\pm}$ ($\mathrm{pp} \to \mathrm{H}^{\pm}\mathrm{W}^{\mp}\mathrm{b\bar{b}}$) for masses larger (smaller) than the top quark ($m_{\mathrm{H}^{\pm}} > m_{\mathrm{t}} - m_{\mathrm{b}}$) and focuses on the fully hadronic final state. Figure 1 shows examples of Feynman diagrams of the production mode for the light- and heavy-mass scenarios.

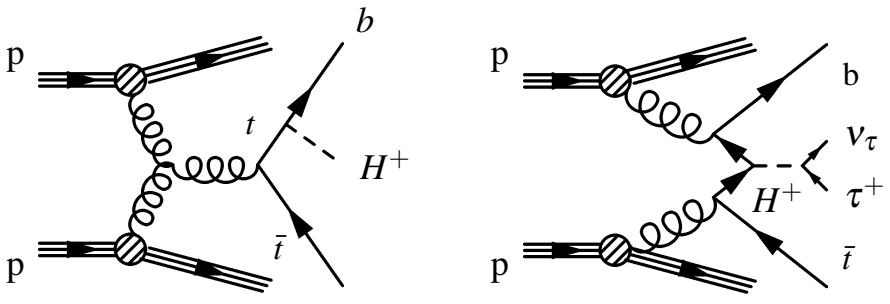

Figure 1: Examples of charged Higgs boson ($\mathrm{H}^{\pm}$) production diagrams for the light-mass scenario as part of the decay of the top quark (**left**) and for the heavy mass scenario in association with top and bottom quark (**right**).

2 The CMS experiment

The central feature of the CMS apparatus is a superconducting solenoid of 6 m internal diameter, providing a magnetic field of 3.8 T. Within the solenoid volume are a silicon pixel and strip tracker, a lead tungstate crystal electromagnetic calorimeter (ECAL), and a brass and scintillator hadron calorimeter (HCAL), each composed of a barrel and two endcap sections. Forward calorimeters extend the pseudorapidity coverage up to $|\eta| = 5$ coverage by the barrel and endcap detectors. Muons are measured in gas-ionization detectors embedded in the steel flux-return yoke outside the solenoid.

The silicon tracker measures charged particles within the pseudorapidity range $|\eta| < 2.5$. It consists of 1440 silicon pixel and 15 148 silicon strip detector modules and is located in the field of the superconducting solenoid. For nonisolated particles of $1 < p_T < 10$ GeV and $|\eta| < 1.4$, the track resolutions are typically 1.5% in p_T and 25–90 (45–150) μm in the transverse (longitudinal) impact parameter [21]

In the region $|\eta| < 1.74$, the HCAL cells have widths of 0.087 in pseudorapidity and 0.087 in azimuth (ϕ). In the η–ϕ plane, and for $|\eta| < 1.48$, the HCAL cells map on to 5×5 arrays of ECAL crystals to form calorimeter towers projecting radially outwards from close to the nominal interaction point. For $|\eta| > 1.74$, the coverage of the towers increases progressively to a maximum of 0.174 in $\Delta\eta$ and $\Delta\phi$. Within each tower, the energy deposits in ECAL and HCAL cells are summed to define the calorimeter tower energies, subsequently used to provide the energies and directions of hadronic jets. Using both ECAL and HCAL, the jet energy resolution amounts typically to 40% at 10 GeV, 12% at 100 GeV, and 5% at 1 TeV. When combining the information with the tracker, the jet energy resolution is improved to 15%, 8%, and 4% respectively.

The first level (L1) of the CMS trigger system, composed of custom hardware processors, uses information from the calorimeters and muon detectors to select events of interest within a time interval of less than 4 μs. The high-level trigger (HLT) processor farm reduces the event rate from the around 100 kHz provided by the L1 trigger to less than 1 kHz, before data storage.

A more detailed description of the CMS detector, together with a definition of the coordinate system used and the relevant kinematic variables, can be found in Ref. [22].

3 Data and simulation events

The analysis is performed using the data collected in the first part of 2016 by the CMS experiment that correspond to an integrated luminosity of 12.9 fb^{-1}.

The signal processes are generated with MadGraph5_aMC@NLO [23] for the masses ranging from 80 GeV to 3 TeV, with the production mode $pp \to tbH^{\pm}$ ($pp \to H^{\pm}W^{\mp}b\bar{b}$) for charged Higgs bosons with mass above (below) $m_t - m_b$.

The background processes include the simulation of top-pair production ($t\bar{t}$), single top production at next-to-leading order (NLO) [24–27], the Drell–Yan production [23], the W+jets production at leading order (LO) in quantum chromodynamics (QCD) with up to 4 associated partons [28], and the diboson production [23, 29]. Data driven methods are used to validate or estimate these backgrounds in the considered phase-space region as described below.

The parton showering and the hadronization, as well as the underlying event, are modelled with PYTHIA 8.1 [30] with the Tune CUETP8M1 [31].

The simulation of the CMS detector is based on the GEANT4 package [32]. The simulated events are reconstructed following the same procedures used for the data. Multiple inelastic proton-proton collisions occur per LHC bunch-crossing (in-time pileup) and are added to the simulation, as well as inelastic collisions happening in the preceding and subsequent bunch crossings (out-of-time pileup).

4 Event Reconstruction

Event reconstruction is based on a particle-flow (PF) algorithm [33, 34], combining information from all CMS subdetectors to reconstruct individual particle candidates: muons, electrons, photons, charged and neutral hadrons. Complex objects such as jets, hadronically decaying τ leptons, and missing transverse energy ($\not\!\!E_T$) are then constructed using the lists of individual particles.

The reconstruction of the collision vertices uses the deterministic annealing algorithm [35]. The vertex having the maximum sum of squared transverse momenta calculated from all associated tracks is considered as the primary vertex of the hard interaction. Muons, electrons, and hadronically decaying τ leptons are required to originate from the primary vertex of the hard interaction. All other vertices are devoted to pileup events.

Electrons are reconstructed by combining clusters of ECAL energy deposits with hits in the silicon tracker [36]. In addition, electrons are required to pass identification requirement based on cluster shape variables, on the fraction of energy deposited in the hadronic calorimeter (HCAL) and on the track direction. Muons are reconstructed by combining tracks from the silicon tracker with hits or standalone tracks reconstructed in the muon system [37].

Conditions are placed on the isolation of the electrons and muons measured relative to their transverse momenta, by summing the charged and neutral particles reconstructed by the PF algorithm. The presence of neutral particles from pileup vertices is taken into account by summing the transverse momenta of charged hadrons from pileup vertices in the isolation cone, and multiplying by a factor of 0.5 to account for the fraction of neutral to charged hadron production. This is then subtracted from the raw isolation.

Jets are reconstructed from PF candidates using the anti-k_{T} jet clustering algorithm implemented in FASTJET [38, 39] with a distance parameter of 0.4. Jets from the hadronization of b quarks (b jets) are identified using the combined secondary vertex (CSV) b-tagging algorithm [40], which exploits the information on the decay vertices of long-lived mesons and the impact parameters of charged particle tracks, combined in a likelihood discriminant.

Hadronically decaying τ leptons are reconstructed using the hadron-plus-strips algorithm [41]. The algorithm considers candidates with one charged pion and up to two neutral pions, or three charged pions, and is seeded by a jet. The neutral pions decay rapidly into two photons, and are reconstructed as "strips" of electromagnetic particles, formed with dynamic size from energy depositions in the ECAL. The τ decay mode is reconstructed by combining the charged hadrons with the ECAL strips. The τ^{h} candidates that are also compatible with muons or electrons are rejected. Jets originating from the hadronization of quarks and gluons are suppressed by requiring the τ^{h} candidate to be isolated. The isolation variable is constructed from the PF-candidates inside a cone of $\Delta R = 0.3$ is used. Pileup contributions to the neutral component are accounted for using tracks coming from the other vertices reconstructed in the event.

The missing transverse momentum vector ($\vec{\not\!\!E}_T$) is defined as the negative vector sum of the transverse momenta of all reconstructed PF particles. Its magnitude is referred to as $\not\!\!E_T$ [42].

5 Event selection

The events selection starts online requiring the presence of a τ^{h} and large $\not\!\!E_T$. Online trigger requires that a loosely isolated hadronic tau with $p_{\mathrm{T}}^{\tau^{\mathrm{h}}} > 50$ GeV and $|\eta^{\tau^{\mathrm{h}}}| < 2.1$, that contains a leading charged hadron with $p_{\mathrm{T}} > 30$ GeV, and that the missing transverse energy, reconstructed with the calorimetric information only, has a magnitude of $\not\!\!E_T > 90$ GeV. The efficiency of the τ^{h} and $\not\!\!E_T$ parts of the trigger are measured independently and corrections are propagated to the simulation. Figure 2 shows the efficiency in simulation (prior to the correction) and in data for the τ^{h} and $\not\!\!E_T$ parts of the trigger used in the analysis.

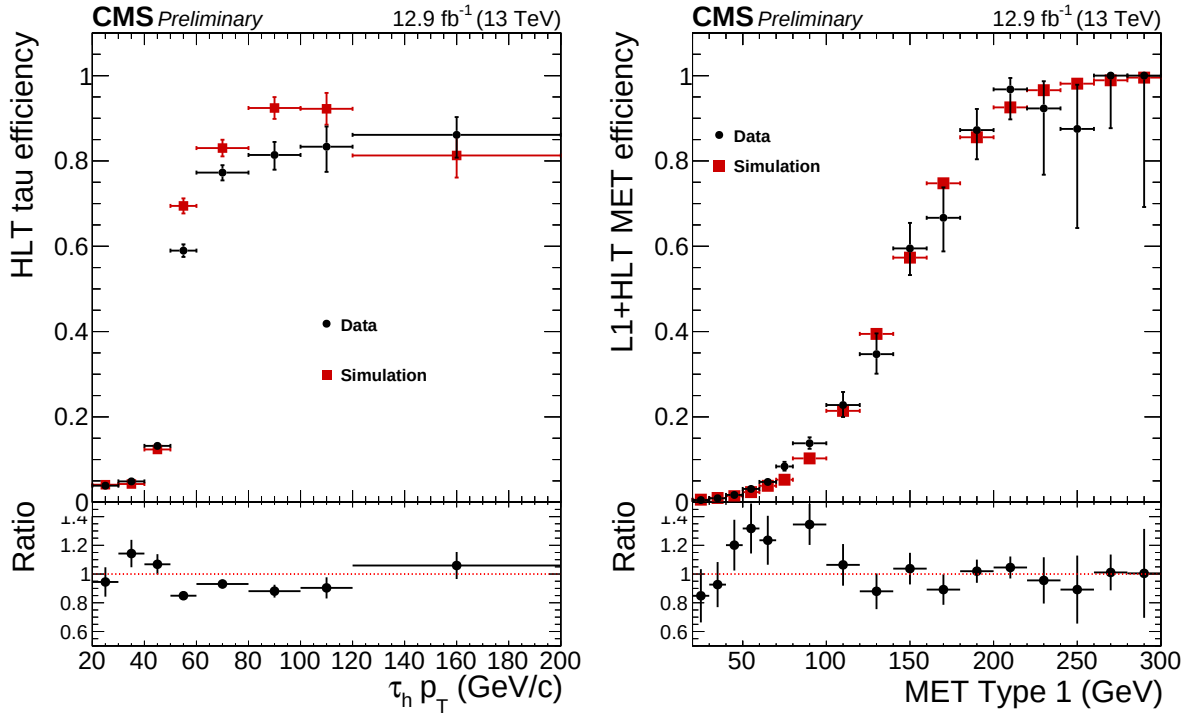

Figure 2: Data/simulation of the trigger efficiency for the hadronic tau transverse momentum (**left**) and the missing transverse energy (**right**) parts of the τ^{h} plus $\not\!\!E_T$ trigger, respectively.

Events are subsequently selected requiring to have offline $p_{\mathrm{T}}^{\tau^{\mathrm{h}}} > 60$ GeV and $\not\!\!E_T > 100$ GeV; for the search region below the top mass, the $\not\!\!E_T$ and $p_{\mathrm{T}}^{\tau^{\mathrm{h}}}$ requirements are made closer to the trigger requirements to $\not\!\!E_T > 90$ GeV and $p_{\mathrm{T}}^{\tau^{\mathrm{h}}} > 50$ GeV in order to have a larger signal acceptance. Additionally, events containing at least one isolated lepton (e, μ) are rejected.

The presence of a signal is further enhanced by requiring at least three reconstructed jets ($N_{\mathrm{jets}} \geq 3$), and in the tracker-covered region one b-tagged jet.

Moreover, the event variable $R_{\mathrm{bb}}^{\mathrm{min}}$ [20] is used to reject multijet events where the $\not\!\!E_T$ and τ^{h} are in a back-to-back configuration. It is defined through the angular correlation among the τ^{h}, the $\not\!\!E_T$, and the three leading jets in the event ($j_1..j_3$) as:

$$R_{\mathrm{bb}}^{\mathrm{min}} = \min_{j \in j_1..j_3} \sqrt{\Delta\phi(\not\!\!E_T, j)^2 + (\pi - \Delta\phi(\tau^{\mathrm{h}}, \not\!\!E_T))^2} \quad (1)$$

Its value is required to be greater than $R_{\mathrm{bb}}^{\mathrm{min}} > 40^\circ$, and the distribution of this variable for events passing the all selection with the exception of the self requirement is presented in Fig. 3.

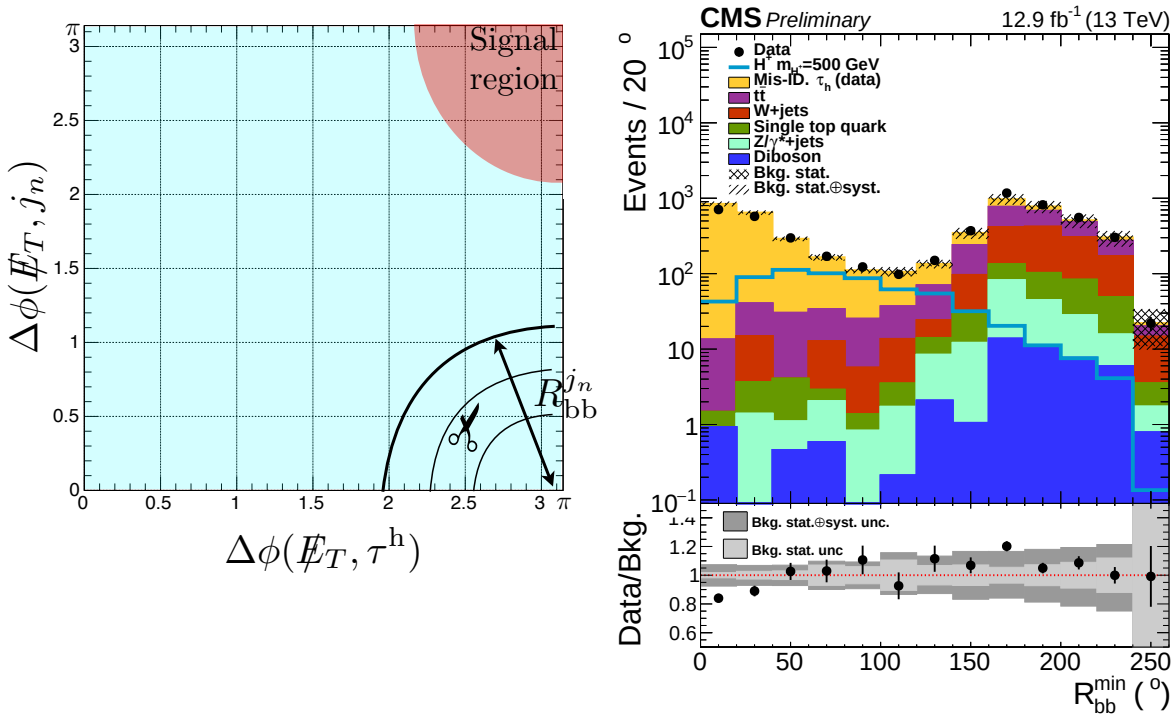

Figure 3: Sketch of the plane $\Delta\phi(\tau^{\mathrm{h}}, \not\!\!E_T)$–$\Delta\phi(\tau^{\mathrm{h}}, j_n)$ and it's connection to the $R_{\mathrm{bb}}^{\mathrm{min}}$ variable (**left**), and the angular variable $R_{\mathrm{bb}}^{\mathrm{min}}$ after the all selection except the self requirement (**right**); the data points (solid black) with their statistical uncertainty (solid lines) are compared to the background predictions split for the different contributions (filled histograms).

The signal extraction is performed with the transverse mass variable (m_{T}), reconstructed from the hadronic tau and $\not\!\!E_T$, and defined as [42]:

$$m_{\mathrm{T}}^2 = 2 \cdot p_{\mathrm{T}}^{\tau^{\mathrm{h}}} |\vec{\not\!\!E}_T| \left(1 - \cos\Delta\phi(\not\!\!E_T, \tau^{\mathrm{h}})\right) \tag{2}$$

The presence of additional neutrinos from the $\tau \to \tau^{\mathrm{h}}$ decay smears the distribution to lower m_{T} values, preserving but making less sharp the end-point expected at $m_{\mathrm{T}} = m_{\mathrm{H}^\pm}$. An additional smearing of this distribution is expected from the width of the charged Higgs, especially large at high values of $m_{\mathrm{H}^\pm}$.

6 Background estimation

The main background process are QCD multijet production, electroweak (EW) processes and events containing top quark(s). We distinguish processes with genuine tau leptons and those with electrons, muons or jets being misidentified as hadronic tau decays.

Data-driven techniques are exploited in order to estimate the misidentified jets faking a hadronic tau. This background comes mostly from the multijet production. The probability of a jet faking a tau is small, but the huge cross section makes this background contribution sizable. Jointly to the lacking of reliable predictions from simulations in this phase space and tau enrichment filters, data-driven techniques are deployed and predictions based on reverting the isolation identification requirements allow for quite good control over these kind of backgrounds.

The background with misidentified tau leptons is measured by selecting events which are enriched in this contribution, by reverting the isolation requirements on the hadronic taus (inverted selection). In order to normalize this contribution to the one with at least one isolated

tau (baseline selection), the fraction of the multijet events in the baseline selection is estimated as follows: a maximum likelihood fit is performed to the baseline $\not\!\!E_T$ distribution in the signal region; the $\not\!\!E_T$ distribution of the EW+$t\bar{t}$ background with misidentified taus is taken from simulation, while the $\not\!\!E_T$ shape of the distribution of the multijet component is fitted in the inverted selection. The large contribution from genuine taus coming from the EW and $t\bar{t}$ processes is accounted for. The normalization of the multijet events, dominated by gluon jets, is achieved by dividing the number of the multijet events, estimated through the fit, in the baseline selection by the number of multijet events in the inverted selection. The normalization for EW and $t\bar{t}$ events with no genuine taus is determined from simulation. The overall normalization of the data in the inverted selection is taken as a sum of the multijet and EW+$t\bar{t}$ misidentified tau normalization factors weighted by their relative fractions. In the estimation of the misidentified tau background, the genuine tau component, taken from simulation, is subtracted from the inverted data. In order to take any possible correlations into account, these factors are derived separately in bins of tau transverse momentum.

Figure 4 shows the sequential selection requirement yields showing a good control of the event flow across the different selections.

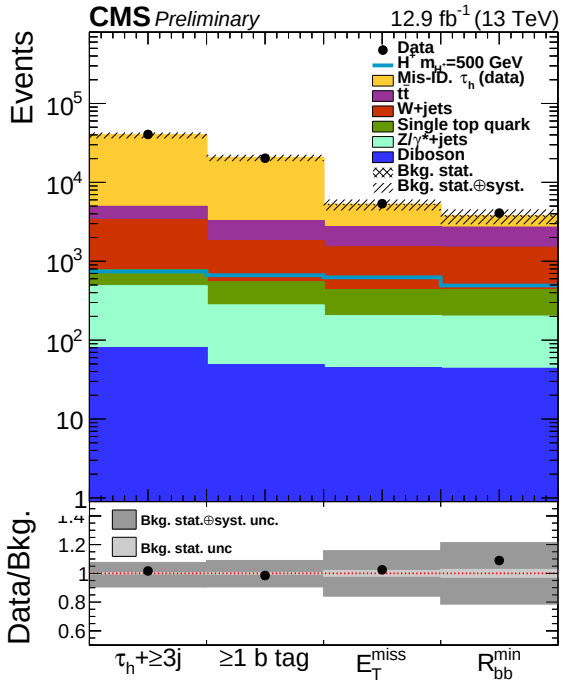

Figure 4: Sequential selection requirements in the high mass analysis comparing background predictions to data.

Electroweak processes and top production are evaluated using simulations. Drell–Yan (DY), W boson productions in association with jets, diboson (WW, WZ, ZZ) productions, as well as single top and top pair productions are taken into account. These production processes have been validated requiring in the selection an isolated muon, instead of the selected tau lepton, considering the expected differences in efficiencies and reconstruction, and data agree with the simulation.

7 Systematic uncertainties

Systematic uncertainties account for possible mispredictions in the observables used in the analysis.

The uncertainty associated to the measurement of the luminosity is propagated to the simulation and amounts to 6.2%. Possible inaccuracies in the jet energy scale (JES) and in the jet energy resolution (JER) are considered as well. The uncertainty associated to the corresponding quantities is propagated to the final selection, allowing to modify both the number of associated jets and the estimation of the missing transverse energy. The uncertainties in the efficiency of the b-tagging algorithm, as well as its misidentification rate are separately propagated to the analysis as scale factors.

The data/simulation agreement in the hadronic tau identification has been evaluated with different techniques. The inaccuracies associated to this measurement are accounted for in the analysis, and conservatively amount to 10%. An additional uncertainty is associated to the extrapolation of these scale factors at very large p_{T} that values $20\% \cdot p_{\mathrm{T}}/1\mathrm{TeV}$. The energy scale of the hadronic taus is known within 3%, and corresponding shifts in the template used and their correlation with the $\not\!\!E_T$ are accounted as nuisances in the limit extraction.

Trigger efficiencies are measured in data, as discussed in Section 5, and discrepancies are propagated to the simulation in form of variations on the scale factors, and to the analysis flow.

The data driven estimation of the misidentified taus is subject to uncertainties due to possible model assumptions in the background to be estimated; All errors associated to the fits used in the method are considered. Moveover, possible discrepancies of the $\not\!\!E_T$ distribution raising from intrinsic differences in the energy flow of the events as well as its composition are accounted for in the analysis.

The cross sections used to normalize the simulated contributions are allowed to vary within the theory uncertainties and they include parton density function (PDF) and scale uncertainty for top pair and single top productions, Drell–Yan and W+jets, and diboson productions. An additional term in the $\mathrm{t\bar{t}}$ and single top production cross sections is due to possible inaccuracies of the top mass used in the calculations. Furthermore, statistical uncertainty on the simulations and on the data-driven predictions are accounted as bin-by-bin nuisance parameters.

The efficiency of the lepton veto requirement is measured in data using the tag and probe method. Differences in reconstruction and isolation efficiencies between data and MC are propagated to the simulation as scale factors, and uncertainties on this estimation are accounted as possible source of systematic effects in the analysis.

The dominant source of uncertainty in the high mass spectrum is due to the data set size, while systematic effects become more and more important at lower masses. The dominant source of uncertainties are related to the τ^{h}, the jet and the $\not\!\!E_T$ energy scales, through their impact on the m_{T} distribution and the total number of events observed, followed up by the uncertainties on the misidentified τ^{h} predictions and on the top spectrum. Furthermore, a modest contribution of the MC data set size is seen in the analysis. All other systematic effects have a small impact on the final result.

8 Results

Events yields after the selection flow are reported in Table 1, where the data are compared to expectation from simulation before the fit.

Table 1: Number of selected events for the low-mass and high-mass searches in data and corresponding predictions for the 2016 data-taking periods.

	Yields ($m_{H^\pm} < m_t - m_b$)	Yields ($m_{H^\pm} > m_t - m_b$)
EW	1454.3	1151.7
Top	1792.9	1318.4
Fake-τ^h	2564.4	1197.8
Tot	5811.6	3667.9
Data	6276	4179

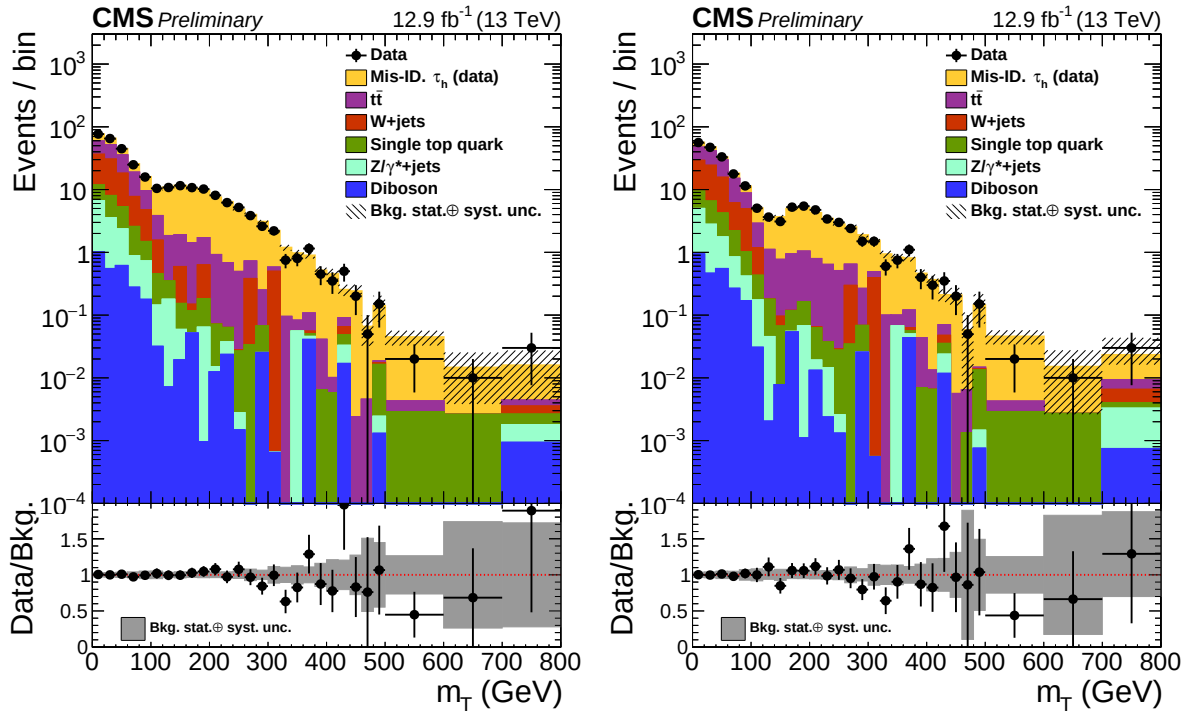

Figure 5: The m_T distribution in data compared to the post-fit background predictions for the low- (**left**) and high-mass (**right**) search selection.

A binned maximum likelihood fit is performed to the m_{T} distribution, in order to extract the signal. The fit to the m_{T} distribution is shown in Fig. 5 for the low- and high-mass searches selections. The fit is carried out both in the background-only and signal+background scenarios, and the 95% confidence level (CL) limits are set on the production cross-section using the $\mathrm{CL_s}$ criterion [43, 44] on the likelihood ratio test-statistics [45, 46].

Model independent limits on the branching fraction of $\mathcal{B}(\mathrm{t} \to \mathrm{bH}^{\pm}) \times \mathcal{B}(\mathrm{H}^{\pm} \to \tau^{\pm}\nu_{\tau})$ are shown in Fig. 6 (left) for the mass range between 80–160 GeV, while in Fig. 6 (right) the model independent limits on the production cross section $\sigma(\mathrm{pp} \to \mathrm{tbH}^{\pm})$ at $\sqrt{s} = 13\,\mathrm{TeV}$ times the branching fraction $\mathcal{B}(\mathrm{H}^{\pm} \to \tau^{\pm}\nu_{\tau})$ are presented for masses in the range 180 GeV–3 TeV.

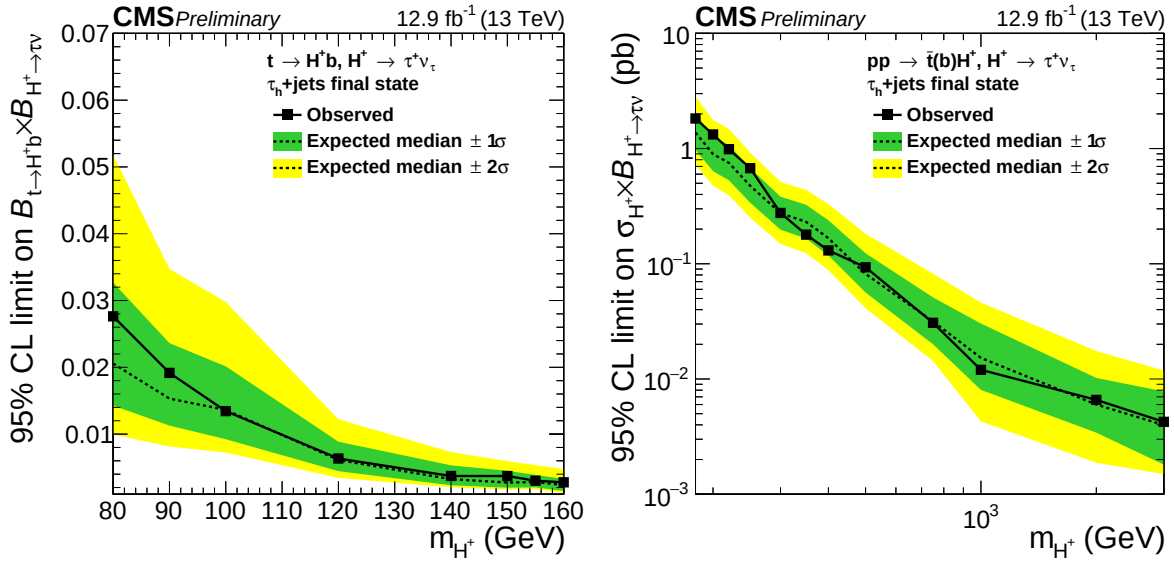

Figure 6: The observed 95 % CL exclusion limits (solid points) on $\mathcal{B}(\mathrm{t} \to \mathrm{bH}^{\pm}) \cdot \mathcal{B}(\mathrm{H}^{\pm} \to \tau^{\pm}\nu_{\tau})$ (**left**) and $\sigma(\mathrm{pp} \to \mathrm{H}^{\pm}\mathrm{W}^{\mp}\mathrm{b}\bar{\mathrm{b}}) \cdot \mathcal{B}(\mathrm{H}^{\pm} \to \tau^{\pm}\nu_{\tau})$ (**right**) is compared to the expectations from the SM model (dashed line). The green (yellow) error bands represent one (two) standard deviations of the expected limit.

The limits are compatible with the SM expectations of a background only hypothesis. Limits are interpreted in the context of the m_h^{mod+} benchmark scenario [47]. The excluded region of the ($m_{\mathrm{H}^{\pm}}$, $\tan\beta$) parameter space at 95% CL is shown in Fig. 7. Since the production cross section times branching fraction enhances at large $\tan\beta$, the high $\tan\beta$ region is consequently excluded.

9 Summary

We presented a search for charged Higgs bosons decaying to $\mathrm{H}^{\pm} \to \tau^{\pm}\nu_{\tau}$ in the fully hadronic final state. The charged Higgs bosons can be produced in top quark decays $\mathrm{pp} \to \mathrm{H}^{\pm}\mathrm{W}^{\mp}\mathrm{b}\bar{\mathrm{b}}$, if the charged Higgs boson is lighter than the top quark, or via direct production $\mathrm{pp} \to \mathrm{t(b)H}^{\pm}$ in association with a top quark at high masses. In both cases the experimental final state is similar. The search is performed using data collected in 2016 by CMS at $\sqrt{s} = 13$ TeV, corresponding to a total integrated luminosity of $12.9\,\mathrm{fb}^{-1}$. The observation agrees with the standard model prediction. Model independent limits on charged Higgs bosons branching fraction $\mathcal{B}(\mathrm{t} \to \mathrm{H}^{\pm}\mathrm{b}) \times \mathcal{B}(\mathrm{H}^{\pm} \to \tau\nu)$ and the cross section times branching fraction $\sigma_{\mathrm{pp}\to\mathrm{t(b)H}^{\pm}} \times \mathcal{B}(\mathrm{H}^{\pm} \to \tau\nu)$ are given for the mass ranges of 80 GeV $< m_{\mathrm{H}^{\pm}} <$ 160 GeV and 180 GeV $< m_{\mathrm{H}^{\pm}} <$ 3 TeV, respectively. The results are interpreted in the context of the MSSM m_h^{mod+} benchmark scenario.

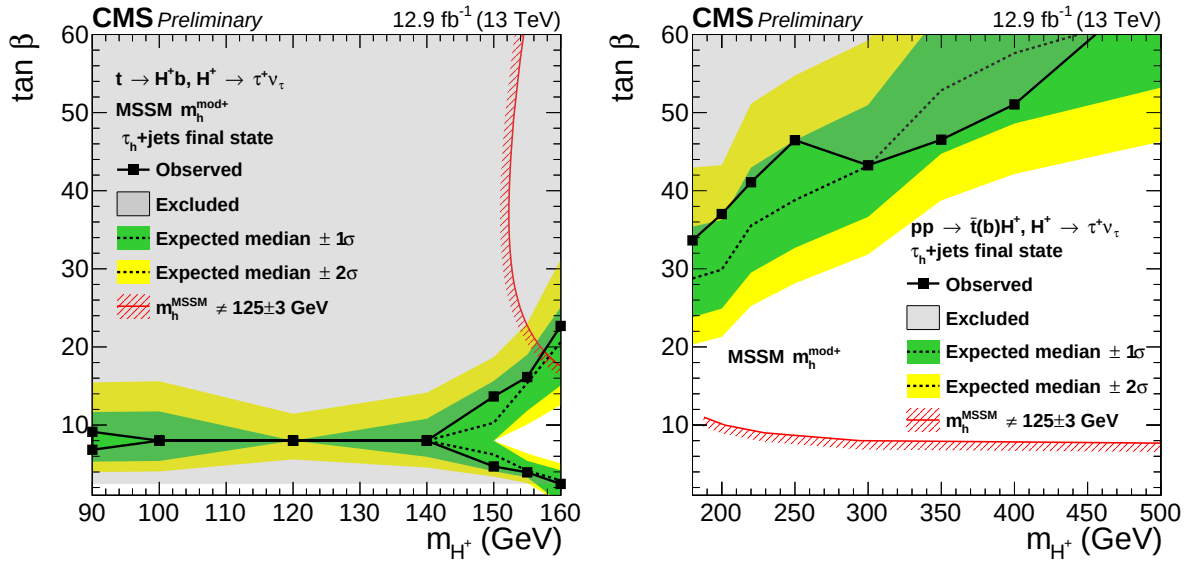

Figure 7: Exclusion limits in the $m_{\mathrm{H}^{\pm}}$–tan β plane in the context of the mh-mod+ model, for the low mass search (**left**) and the high mass search (**right**).

References

[1] ATLAS Collaboration, "Observation of a new particle in the search for the Standard Model Higgs boson with the ATLAS detector at the LHC", *Phys. Lett. B* **716** (2012) 1–29, doi:10.1016/j.physletb.2012.08.020, arXiv:1207.7214.

[2] CMS Collaboration, "Observation of a new boson at a mass of 125 GeV with the CMS experiment at the LHC", *Phys. Lett. B* **716** (2012) 30–61, doi:10.1016/j.physletb.2012.08.021, arXiv:1207.7235.

[3] CMS Collaboration, "Precise determination of the mass of the Higgs boson and tests of compatibility of its couplings with the standard model predictions using proton collisions at 7 and 8 TeV", *Eur. Phys. J. C* **75** (2015), no. 5, 212, doi:10.1140/epjc/s10052-015-3351-7, arXiv:1412.8662.

[4] ATLAS Collaboration, "Study of the spin and parity of the Higgs boson in diboson decays with the ATLAS detector", *Eur. Phys. J. C* **75** (2015), no. 10, 476, doi:10.1140/epjc/s10052-015-3685-1, arXiv:1506.05669.

[5] CMS Collaboration, "Constraints on the spin-parity and anomalous HVV couplings of the Higgs boson in proton collisions at 7 and 8 TeV", *Phys. Rev. D* **92** (2015), no. 1, 012004, doi:10.1103/PhysRevD.92.012004, arXiv:1411.3441.

[6] F. Englert and R. Brout, "Broken Symmetry and the Mass of Gauge Vector Mesons", *Phys. Rev. Lett.* **13** (1964) 321, doi:10.1103/PhysRevLett.13.321.

[7] P. W. Higgs, "Broken symmetries, massless particles and gauge fields", *Phys. Lett.* **12** (1964) 132, doi:10.1016/0031-9163(64)91136-9.

[8] P. W. Higgs, "Broken Symmetries and the Masses of Gauge Bosons", *Phys. Rev. Lett.* **13** (1964) 508, doi:10.1103/PhysRevLett.13.508.

[9] G. S. Guralnik, C. R. Hagen, and T. W. B. Kibble, "Global Conservation Laws and Massless Particles", *Phys. Rev. Lett.* **13** (1964) 585, doi:10.1103/PhysRevLett.13.585.

[10] P. W. Higgs, "Spontaneous Symmetry Breakdown without Massless Bosons", *Phys. Rev.* **145** (1966) 1156, doi:10.1103/PhysRev.145.1156.

[11] T. W. B. Kibble, "Symmetry breaking in non-Abelian gauge theories", *Phys. Rev.* **155** (1967) 1554, doi:10.1103/PhysRev.155.1554.

[12] N. Craig and S. Thomas, "Exclusive signals of an extended Higgs sector", *Journal of High Energy Physics* **2012** (2012), no. 11, 1–28, doi:10.1007/JHEP11(2012)083.

[13] G. C. Branco et al., "Theory and phenomenology of two-Higgs-doublet models", *Phys. Rept.* **516** (2012) 1–102, doi:10.1016/j.physrep.2012.02.002, arXiv:1106.0034.

[14] A. Djouadi, "The Anatomy of electro-weak symmetry breaking. II. The Higgs bosons in the minimal supersymmetric model", *Phys. Rept.* **459** (2008) 1–241, doi:10.1016/j.physrep.2007.10.005, arXiv:hep-ph/0503173.

[15] Ch. Englert, E. Re, and M. Spannowsky, "Triplet Higgs boson collider phenomenology after the LHC", *Phys. Rev. D* **87** (2013) 095014, doi:10.1103/PhysRevD.87.095014, arXiv:1302.6505.

[16] Ch. Englert, E. Re, and M. Spannowsky, "Pinning down Higgs triplets at the LHC", *Phys. Rev. D* **88** (2013) 035024, doi:10.1103/PhysRevD.88.035024, arXiv:1306.6228.

[17] LEP, DELPHI, OPAL, ALEPH, L3 Collaboration, "Search for Charged Higgs bosons: Combined Results Using LEP Data", *Eur. Phys. J.* **C73** (2013) 2463, doi:10.1140/epjc/s10052-013-2463-1, arXiv:1301.6065.

[18] CDF Collaboration, "Search for Higgs bosons predicted in two-Higgs-doublet models via decays to tau lepton pairs in 1.96-TeV p anti-p collisions", *Phys. Rev. Lett.* **103** (2009) 201801, doi:10.1103/PhysRevLett.103.201801, arXiv:0906.1014.

[19] D0 Collaboration, "Search for Higgs bosons of the minimal supersymmetric standard model in $p\bar{p}$ collisions at $\sqrt(s) = 1.96$ TeV", *Phys. Lett.* **B710** (2012) 569–577, doi:10.1016/j.physletb.2012.03.021, arXiv:1112.5431.

[20] CMS Collaboration, "Search for a charged Higgs boson in pp collisions at $\sqrt{s} = 8$ TeV", *JHEP* **11** (2015) 018, doi:10.1007/JHEP11(2015)018, arXiv:1508.07774.

[21] CMS Collaboration, "Description and performance of track and primary-vertex reconstruction with the CMS tracker", *JINST* **9** (2014) P10009, doi:10.1088/1748-0221/9/10/P10009, arXiv:1405.6569.

[22] CMS Collaboration, "The CMS experiment at the CERN LHC", *JINST* **3** (2008) S08004, doi:10.1088/1748-0221/3/08/S08004.

[23] J. Alwall et al., "The automated computation of tree-level and next-to-leading order differential cross sections, and their matching to parton shower simulations", *JHEP* **07** (2014) 079, doi:10.1007/JHEP07(2014)079, arXiv:1405.0301.

[24] S. Alioli, P. Nason, C. Oleari, and E. Re, "NLO single-top production matched with shower in POWHEG: s- and t-channel contributions", *JHEP* **09** (2009) 111, doi:10.1007/JHEP02(2010)011, 10.1088/1126-6708/2009/09/111, arXiv:0907.4076. [Erratum: JHEP02,011(2010)].

[25] S. Alioli, P. Nason, C. Oleari, and E. Re, "NLO single-top production matched with shower in POWHEG: s- and t-channel contributions", *JHEP* **09** (2009) 111, doi:10.1007/JHEP02(2010)011, 10.1088/1126-6708/2009/09/111, arXiv:0907.4076. [Erratum: JHEP02,011(2010)].

[26] E. Re, "Single-top Wt-channel production matched with parton showers using the POWHEG method", *Eur. Phys. J.* **C71** (2011) 1547, doi:10.1140/epjc/s10052-011-1547-z, arXiv:1009.2450.

[27] T. Jeo et al., "An NLO+PS generator for $t\bar{t}$ and Wt production and decay including non-resonant and interference effects", arXiv:1607.04538.

[28] J. Alwall et al., "MadGraph 5 : Going Beyond", *JHEP* **06** (2011) 128, doi:10.1007/JHEP06(2011)128, arXiv:1106.0522.

[29] P. Nason and G. Zanderighi, "W^+W^- , WZ and ZZ production in the POWHEG-BOX-V2", *Eur. Phys. J.* **C74** (2014), no. 1, 2702, doi:10.1140/epjc/s10052-013-2702-5, arXiv:1311.1365.

[30] T. Sjostrand, S. Mrenna, and P. Z. Skands, "A Brief Introduction to PYTHIA 8.1", *Comput. Phys. Commun.* **178** (2008) 852–867, doi:10.1016/j.cpc.2008.01.036, arXiv:0710.3820.

[31] CMS Collaboration, "Event generator tunes obtained from underlying event and multiparton scattering measurements", *Eur. Phys. J.* **C76** (2016), no. 3, 155, doi:10.1140/epjc/s10052-016-3988-x, arXiv:1512.00815.

[32] GEANT4 Collaboration, "GEANT4: A Simulation toolkit", *Nucl. Instrum. Meth.* **A506** (2003) 250–303, doi:10.1016/S0168-9002(03)01368-8.

[33] CMS Collaboration, "Particle–Flow Event Reconstruction in CMS and Performance for Jets, Taus, and $E_{\mathrm{T}}^{\mathrm{miss}}$", CMS Physics Analysis Summary CMS-PAS-PFT-09-001, 2009.

[34] CMS Collaboration, "Commissioning of the Particle-flow Event Reconstruction with the first LHC collisions recorded in the CMS detector", CMS Physics Analysis Summary CMS-PAS-PFT-10-001, 2010.

[35] K. Rose, "Deterministic annealing for clustering, compression, classification, regression, and related optimization problems", *Proceedings of the IEEE* **86** (Nov, 1998) 2210–2239, doi:10.1109/5.726788.

[36] CMS Collaboration, "Performance of electron reconstruction and selection with the CMS detector in proton-proton collisions at $\sqrt{s} = 8$ TeV", *JINST* **10** (2015) P06005, doi:10.1088/1748-0221/10/06/P06005, arXiv:1502.02701.

[37] CMS Collaboration, "Performance of CMS muon reconstruction in pp collision events at $\sqrt{s} = 7$ TeV", *JINST* **7** (2012) P10002, doi:10.1088/1748-0221/7/10/P10002, arXiv:1206.4071.

[38] M. Cacciari, G. P. Salam, and G. Soyez, "FastJet user manual", *Eur. Phys. J. C* **72** (2012) 1896, doi:10.1140/epjc/s10052-012-1896-2, arXiv:1111.6097.

[39] M. Cacciari and G. P. Salam, "Dispelling the N^3 myth for the k_t jet-finder", *Phys. Lett. B* **641** (2006) 57, doi:10.1016/j.physletb.2006.08.037, arXiv:hep-ph/0512210.

[40] CMS Collaboration, "Identification of b-quark jets with the CMS experiment", *JINST* **8** (2013) P04013, doi:10.1088/1748-0221/8/04/P04013, arXiv:1211.4462.

[41] CMS Collaboration, "Reconstruction and identification of τ lepton decays to hadrons and ν_τ at CMS", *JINST* **11** (2016), no. 01, P01019, doi:10.1088/1748-0221/11/01/P01019, arXiv:1510.07488.

[42] Particle Data Group Collaboration, "Review of Particle Physics", *Chin. Phys.* **C38** (2014) 090001, doi:10.1088/1674-1137/38/9/090001.

[43] A. L. Read, "Presentation of search results: the CLs technique", *J. Phys.* **G28** (2002) 2693, doi:10.1088/0954-3899/28/10/313.

[44] T. Junk, "Confidence level computation for combining searches with small statistics", *Nucl. Instrum. Meth.* **A434** (1999) 435, arXiv:9902006.

[45] "Procedure for the LHC Higgs boson search combination in summer 2011", Technical Report ATL-PHYS-PUB-2011-011, CERN, Geneva, Aug, 2011.

[46] L. Moneta et al., "The RooStats Project", in *13th International Workshop on Advanced Computing and Analysis Techniques in Physics Research (ACAT2010)*. SISSA, 2010. arXiv:1009.1003. PoS(ACAT2010)057.

[47] M. Carena et al., "MSSM Higgs Boson Searches at the LHC: Benchmark Scenarios after the Discovery of a Higgs-like Particle", *Eur. Phys. J.* **C73** (2013), no. 9, 2552, doi:10.1140/epjc/s10052-013-2552-1, arXiv:1302.7033.